A&A, 699, A121 (2025)
https://doi.org/10.1051/0004-6361/202554798
© The Authors 2025

Astronomy & Astrophysics

Inferring chromospheric velocities in an M3.2 flare using He I 1083.0 nm and Ca II 854.2 nm

C. Kuckein[1,2,⋆], M. Collados[1,2], A. Asensio Ramos[1,2], C. J. Díaz Baso[3,4], T. Felipe[1,2], C. Quintero Noda[1,2], L. Kleint[5], L. Fletcher[6,3,4], and S. Matthews[7]

[1] Instituto de Astrofísica de Canarias (IAC), Vía Láctea s/n, E-38205 La Laguna, Tenerife, Spain
[2] Departamento de Astrofísica, Universidad de La Laguna, E-38206 La Laguna, Tenerife, Spain
[3] Institute of Theoretical Astrophysics, University of Oslo, P.O. Box 1029 Blindern, N-0315 Oslo, Norway
[4] Rosseland Centre for Solar Physics, University of Oslo, P.O. Box 1029 Blindern, N-0315 Oslo, Norway
[5] Astronomical Institute of the University of Bern, Sidlerstrasse 5, 3012 Bern, Switzerland
[6] School of Physics and Astronomy, University of Glasgow, Glasgow G12 8QQ, UK
[7] UCL Mullard Space Science Laboratory, Holmbury St Mary, Dorking RH5 6NT, UK

Received 27 March 2025 / Accepted 30 May 2025

ABSTRACT

Aims. Our aim was to study the chromospheric line-of-sight (LOS) velocities during the GOES M3.2 flare (SOL2013-05-17T08:43) using simultaneous high-resolution ground-based spectroscopic data of the He I 10830 Å triplet and Ca II 8542 Å line. A filament was present in the flaring area.

Methods. The observational data were acquired with the Vacuum Tower Telescope (VTT, Tenerife, Spain) and covered the pre-flare, flare, and post-flare phases. Spectroscopic inversion techniques (HAZEL and STiC) were applied individually to He I and Ca II lines to recover the atmospheric parameters of the emitting plasma. Different inversion configurations were tested for Ca II, and two families of solutions were found to explain the red-asymmetry of the profiles: a redshifted emission feature or a blueshifted absorption feature. These solutions could explain two different flare scenarios (condensation vs. evaporation). The ambiguity was solved by comparing these results to the He I inferred velocities.

Results. At the front of the flare ribbon, we observed a thin short-lived blueshifted layer. This is seen in both spectral regions, but is much more pronounced in He I, with velocities of up to $-10\,\mathrm{km\,s^{-1}}$. In addition, at the front we found the coexistence of multiple He I profiles within one pixel. The central part of the ribbon is dominated by He I and Ca II redshifted emission profiles. A flare-loop system, visible only in He I absorption and not in Ca II, becomes visible in the post-flare phase and shows strong downflows at the footpoints of up to $39\,\mathrm{km\,s^{-1}}$. In the flare the Ca II line represents lower heights compared to the quiet Sun, with peak sensitivity shifting from $\log\tau \simeq -5.2$ to $\log\tau \simeq -3.5$. The loop system's downflows persist for over an hour in the post-flare phase.

Conclusions. The inferred LOS velocities support a cool-upflow scenario at the leading edge of the flare, with rapid transition from blueshifts to redshifts likely to occur within seconds to tens of seconds. Although the flare had a significant impact on the surrounding atmosphere, the solar filament in the region remained stable throughout all flare phases. The inclusion of the He I triplet in the analysis helped resolve the ambiguity between two possible solutions for the plasma velocities detected in the Ca II line. This highlights the importance of combining multiple chromospheric spectral lines to achieve a more comprehensive understanding of flare dynamics.

Key words. methods: data analysis – techniques: spectroscopic – Sun: activity – Sun: chromosphere – Sun: flares

1. Introduction

Solar flares are among the most energetic phenomena in our Solar System; they are characterized by a sudden and intense brightening across multiple wavelength ranges in the solar spectrum. These events are triggered in the corona by the reconfiguration of the magnetic field, resulting in the rapid release of enormous amounts of stored magnetic energy (Priest & Forbes 2002; Fletcher et al. 2011). During flares, this energy is converted into thermal energy, radiation across the electromagnetic spectrum, and kinetic energy manifested as plasma flows and particle acceleration. Understanding the dynamics of these plasma flows is crucial to understanding the mechanisms of energy transport and dissipation during flares.

The chromosphere plays an important role during flares (Hudson 2007; Milligan 2015). A significant part of the flare energy goes into continuum radiation, but the exact distribution of the energy conversion is not well known (Milligan et al. 2014; Kleint et al. 2016). This chromosphere undergoes dramatic changes in its thermodynamic properties and flow patterns during flares. Chromospheric evaporation and condensation–the upward and downward flows of plasma in response to the flare–have been studied using spectroscopic observations (Zarro et al. 1988; Keys et al. 2011; Yadav et al. 2021). For instance, the Hα line exhibits red- and blueshifts of $17\,\mathrm{km\,s^{-1}}$ in a C-class flare (Keys et al. 2011).

Among the most popular chromospheric lines for flare-analysis are the Hα and Ca II 8542 Å lines, as well as the He I 10830 Å triplet. In this work we concentrate on the latter two. The Ca II 8542 Å spectral line is of particular interest, as it

⋆ Corresponding author: ckuckein@iac.es

Open Access article, published by EDP Sciences, under the terms of the Creative Commons Attribution License (https://creativecommons.org/licenses/by/4.0), which permits unrestricted use, distribution, and reproduction in any medium, provided the original work is properly cited.
This article is published in open access under the Subscribe to Open model. Subscribe to A&A to support open access publication.

has often been used to study flares (Harvey 2012; Kleint 2012, 2017; Kuridze et al. 2017, 2018; Yadav et al. 2022; Vissers et al. 2021; Ferrente et al. 2023, 2024). It is formed under non-local thermodynamical equilibrium (NLTE) conditions and originates from the transition between the upper $^2P_{1/2}$ and lower $^2D_{3/2}$ levels of the ionized Ca II atom. The line is sensitive to plasma conditions from the lower photosphere to the middle chromosphere (e.g., Quintero Noda et al. 2016; Kuckein et al. 2017). However, simulations have shown that during flares the typical formation height of the core of 8542 Å shifts lower in height by a few hundred kilometers (Rubio da Costa et al. 2015; Kerr et al. 2016). The He I 10830 Å triplet, which forms in the upper chromosphere (Avrett et al. 1994), provides complementary information about higher atmospheric layers and often shows emission profiles followed by strong absorption with significant Doppler shifts during flares (Penn & Kuhn 1995; Kuckein et al. 2015a,b; Judge 2015; Anan et al. 2018). Recent space-based high-resolution observations have revealed the spatial and temporal complexity of these flows, including the discovery of localized regions at the leading edges of flare ribbons exhibiting oppositely directed flows compared to the main flare areas (Xu et al. 2016; Tei et al. 2018; Panos et al. 2018; Polito et al. 2023).

Spectral line inversion tools, such as NICOLE (Socas-Navarro et al. 2015), the STockholm inversion Code (STiC, de la Cruz Rodríguez et al. 2019), DeSIRe (Ruiz Cobo et al. 2022), and HAnle and ZEeman Light (HAZEL, Asensio Ramos et al. 2008), are capable of deriving physical parameters from the Ca II 8542 Å line or He I 10830 Å triplet, providing valuable information about the atmosphere where the line originated. It is important to note that Stokes profiles in flares are often highly complex. The stratification inferred from single-line studies is often poorly constrained as different solutions can reproduce the same spectra. Therefore, multi-line studies are necessary for an accurate interpretation (e.g., Díaz Baso et al. 2021), and we aim to demonstrate this in our work.

The relationship between flare energy deposition and the resulting plasma flows is still not fully understood. Numerical models suggest that the magnitude and direction of flows depend on the depth and rate of energy deposition (Fisher et al. 1985; Reep et al. 2015), but comprehensive observational constraints combining multiple spectral lines formed at different heights remain relatively scarce. Additionally, the temporal evolution of flows from the impulsive phase to the gradual phase reveals important information about the flare energy transport mechanisms. By combining observations from different chromospheric lines, we can build a more complete picture of the height-dependent velocity structure during flares.

In this paper we focus on the analysis of high-resolution ground-based spectroscopic data of He I 10830 Å and Ca II 8542 Å during different phases of an M-class flare. We describe the intensity profiles and infer the line-of-sight (LOS) velocities during the flare.

2. Observations

We followed the evolution of active region NOAA 11748 between 07:49 UT and 10:08 UT on 2013 May 17 with the Vacuum Tower Telescope (VTT, von der Lühe 1998) located on Tenerife, Spain. The main target was an AR filament lying on top of the polarity inversion line (PIL) at solar disk coordinates $(x,y) \sim (-540'', 200'')$ and cosine of the heliocentric angle $\mu = \cos\theta \sim 0.8$. During the observations, an M3.2 flare started at 08:43 UT (SOL2013-05-17T08:43:00) and peaked at 08:57 UT. The two-ribbon flare quickly evolved on both sides of the filament and expanded across the whole active region (see Fig. 1).

The setup included the Echelle spectrograph from the VTT to acquire high-resolution intensity spectra centered at the infrared Ca II 8542 Å line with a PCO.4000 CCD camera. The width of the slit was 100 µm and the scanning step 0.″35. The slit was oriented along the terrestrial north–south direction. The pixel size along the slit was 0.″17. The exposure time for the Ca II spectra was 1 s. The Kiepenheuer-Institute Adaptive Optics System (KAOS; Berkefeld et al. 2010) was locked on high-contrast structures, such as pores and small penumbrae, and was crucial in order to improve the observations.

Spectropolarimetric data acquired simultaneously with the Tenerife Infrared Polarimeter (TIP-II; Collados et al. 2007) in the Si I 10827 Å and He I 10830 Å spectral region were analyzed by Kuckein et al. (2015a,b). However, the chromospheric LOS velocities of He I were not studied. For this work we used the data to study the flows during the present flare, combining different chromospheric lines. The details of the He I 10830 Å observations are described in Kuckein et al. (2015a). The key points are mentioned here: the exposure time per slit position was 10 s, and the scanning step and pixel size were the same as for the above-mentioned Ca II 8542 Å observations. The observed spectral range spanned between 10824 and 10835 Å, with a spectral sampling of about 11.1 mÅ px^{-1}.

Four raster scans, covering almost continuously the time between 07:49 and 10:08 UT, were carried out. These maps cover the pre-flare (map 1), impulsive (map 2), and relaxation phases (maps 3 and 4) of the flare. The first map encompassed 220 and 200 steps, for the He I 10830 Å and Ca II 8542 Å observations, respectively. Maps 2, 3, and 4 covered 150 steps with the slit of about 30 min each. A two-pixel binning along the slit was carried out on all data to produce squared pixels. The coverage and common field of view (FOV) of the maps are depicted as white rectangles in Fig. 1.

3. Data reduction and analysis

3.1. He I 10830 Å calibration

The data was corrected for dark-current and flat-field variations across the detector, and the standard polarimetric calibration was also performed (Collados 1999, 2003). The normalized Stokes profiles were computed by dividing them by the spatially averaged continuum in a quiet-Sun area. The spectral range included two telluric lines, which were used for an absolute wavelength calibration, as described by Kuckein et al. (2012) and Martínez Pillet et al. (1997). A three-pixel binning was performed in the spectral dimension to enhance the signal-to-noise ratio. The spectral sampling was therefore ~33.3 mÅ px^{-1}.

3.2. Ca II 8542 Å calibration

Standard dark-current and flat-field corrections were carried out for the Ca II spectra. An average spectrum was computed to compensate the pre-filter transmission. A three-pixel binning in the spectral dimension was performed to enhance the signal-to-noise ratio. The final wavelength grid comprised 400 positions spanning 10 Å with an equidistant spectral step of 25 mÅ px^{-1}. In addition, the spectra were slightly smoothed by convolving them with a normalized Gaussian with a FWHM of about 50 mÅ. As a final step, we performed an intensity calibration of each map

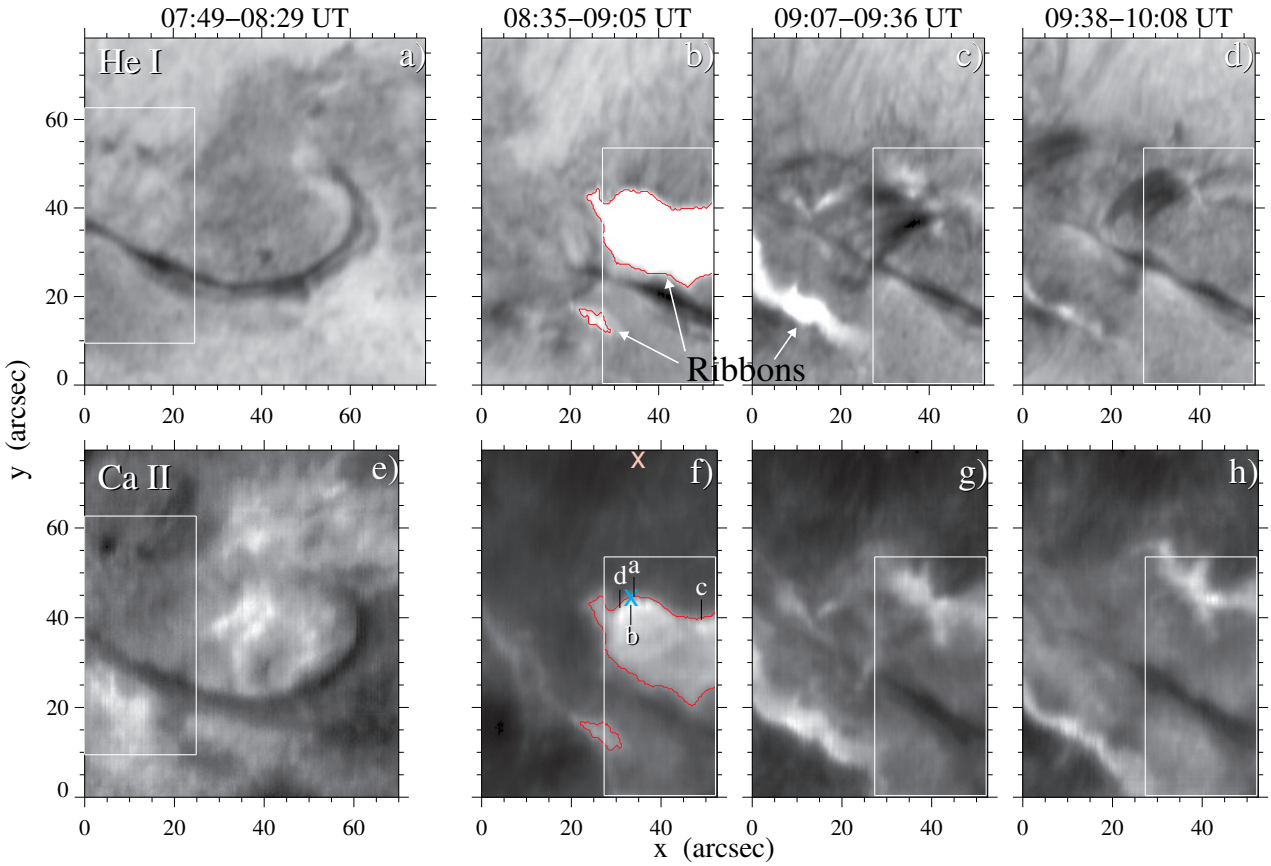

Fig. 1. Slit-reconstructed images of the four raster scans centered at the He I line core of the red component (upper row) and the Ca II line core (lower row). From left to right: pre-flare (panels a and e), flare (panels b and f), and post-flare maps (panels c, d, g, and h). The white box shows the common FOV among all raster scans. The letters a–d in panel f mark the position of the pixels shown in Fig. 4. The light blue and pink crosses in panel f mark the positions of the response functions shown in Fig. 2. The red contours mark the borders of the flare ribbons in panels b and f, using an intensity threshold of $I/I_c = 0.87$ in the line core.

by scaling the intensity in a quiet-Sun area to the spectra from the Fourier Transform Spectra (FTS, Neckel & Labs 1984) spectrometer and taking into account the observed heliocentric angle following Cox (2000), as described in Díaz Baso et al. (2019a). After this, a final inspection showed a residual behavior where the blue wing of the Ca II 8542 Å line systematically exhibited a lower intensity compared to the corresponding continuum at the red side. To address this issue, a solution was implemented by fitting a parabolic function to the ratio of the atlas to the quiet-Sun profile of each scan. In the absence of clearly defined telluric lines, we carried out the wavelength calibration using two lines in the outer blue wing of the Ca II line: (1) the Si I line at 8536.163 Å and (2) the Fe I line at 8538.021 Å (wavelengths taken from Moore & Minnaert 1966).

3.3. He I 10830 Å inversions

The four Stokes parameters were inverted with the inversion code HAZEL[1] to retrieve a model atmosphere. The inversion strategy involved a single chromospheric slab and four cycles, that is, four repetitions of the inversion process per pixel, each using the results of the previous cycle. The first cycle only took into account the intensity profile to find a first solution for the optical depth, Doppler velocity, Doppler width, damping parameter, and a parameter β (see below), which were improved in the following cycles. The remaining three cycles included Stokes Q, U, and V to find a more accurate solution for the above-mentioned parameters taking into account the magnetic field. The β parameter plays an important role when fitting emission profiles on the solar disk. This parameter was introduced ad hoc into HAZEL and multiplied the source function S to produce emission of the He I 10830 Å triplet. HAZEL fits the whole spectral range, including the neighboring Si I 10827 Å and telluric line, in order to account for strong Doppler shifts of the He I triplet. The results of the magnetic field are beyond the scope of this work and will be postponed to a future publication.

3.4. Ca II 8542 Å inversions

We estimated the model atmosphere for the Ca II observations through NLTE inversions. The inversion of the Ca II 8542 Å line was performed using the parallel NLTE code STiC[2], which was based on an optimized version of the RH code (Uitenbroek 2001). Our model was constructed by assuming independent 1D plane-parallel atmospheres along each LOS, an approach commonly referred to as 1.5D modeling.

STiC iteratively adjusts the physical parameters of a model atmosphere, such as the temperature, LOS velocity, magnetic field vector, and microturbulence, to find a synthetic spectrum that reproduces the observed profile. The density and gas

[1] https://github.com/aasensio/hazel2

[2] https://github.com/jaimedelacruz/stic

pressure stratifications are computed by assuming hydrostatic equilibrium (HE). Although HE is likely not valid in flares, it remains the best available approximation. Deviations from HE can introduce uncertainties in the optical depth scale, potentially affecting the absolute location of certain atmospheric features. However, we consider the relative variations between atmospheric layers and the overall trends to be reliable, and thus the main conclusions regarding mass flow patterns remain robust. The physical parameters of the model atmosphere are given as functions of the optical depth scale at 5000 Å, hereafter $\log\tau$. The physical parameters are modified at specific node locations, followed by an interpolation to all other depth points. The merit function that accounts for the likelihood between the synthetic and observed spectra includes an additional regularization term that ensures a smooth behavior in the atmosphere even when a physical parameter has many degrees of freedom (i.e., nodes in the stratification).

We treated the Ca II atom in NLTE with the Ca II 8542 Å line in complete frequency redistribution (CRD). Although STiC can invert the adjacent photospheric lines simultaneously, we did not include them. The reason is that our initial attempts to include the photospheric lines in the STiC inversions produced unsatisfactory results. In particular, it was difficult to achieve a consistent fit for both the broad Ca II 8542 Å line and the much narrower photospheric lines. This mismatch may be attributed to inaccuracies in atomic parameters, differences in line widths requiring careful weighting in the χ^2 minimization, or noise in the weaker photospheric lines. Given our focus on the lower and middle chromosphere, we restricted the inversions to the Ca II line. This implies that our sensitivity to the lower photosphere is diminished, so results around and above ($\log\tau = -1$) should be interpreted with caution. Particularly during the flare peak, there are significant gradients in the velocity stratification that might lead some nodes to reflect small potentially spurious negative velocities at the lower levels where sensitivity is reduced. We initialized the model atmosphere from the FAL-C model (Fontenla et al. 1993) by discretizing it in 81 equidistant depth points from $\log\tau = -6.8$ to $\log\tau = +1.2$. Since the observations were acquired without polarimetry, we set the magnetic field vector to zero. To take into account the spectral degradation of our observations, we used a line spread function (LSF) with a Gaussian shape and a full width at half maximum (FWHM) of 60 mÅ. This value was estimated by comparing the FTS spectrum and our final average quiet-Sun profile. During the inversion we weighted all spectral points equally.

Finally, to investigate the robustness of the solution of the inversion problem, we opted to run the inversions using two different configurations: (a) in multiple cycles of increasing numbers of nodes and (b) in multiple cycles starting with a large number of nodes. The only difference is the number of nodes of the LOS velocity. This allowed us to find two different families of solutions; they are discussed in the following section. The inversion strategies are summarized in Table 1. We note that the large number of nodes required in these inversions, compared to other contemporary studies (e.g., Kuridze et al. 2017), results from the detailed spectral information provided by our slit spectrograph and the dynamic nature of the flare profiles. Nevertheless, the strong regularization applied to the inversion nodes significantly reduces the effective degrees of freedom in the optimization, ensuring a smooth and consistent solution. In summary, since the observations were acquired without polarimetry, we only have as free parameters the temperature (T), the line-of-sight velocity (v_{LOS}), and the microturbulent velocity (v_{turb}). The same configurations were used for the four maps.

Table 1. Number of nodes in each physical parameter for each configuration of the Ca II 8542 Å inversions.

	Cycle 1	Cycle 2
Config. A	T=5, v_{LOS}=2, v_{turb}=1	T=17, v_{LOS}=9, v_{turb}=2
Config. B	T=5, v_{LOS}=9, v_{turb}=1	T=17, v_{LOS}=9, v_{turb}=2

4. Results

In this section we present the results of the plasma flows in the chromosphere during the M-class flare, as inferred from the Doppler velocities from the Ca II 8542 Å line and He I 10830 Å triplet.

4.1. Ca II 8542 Å

The Ca II 8542 Å spectral line yields information from the low to mid-chromosphere in the quiet Sun and quiescent active regions. However, it is known that the height of the chromosphere is different and/or altered during flares. To address this, the response functions (RFs), that is, the sensitivity of the Ca II 8542 Å line to changes in the LOS velocity with height in the atmosphere (given by the optical depth), were computed with STiC. The RFs for a pixel in the quiet Sun and a pixel in the flare ribbon, marked in Fig. 1f, are depicted in Fig. 2. To obtain these RFs, we inverted two pixels and calculated the RFs from the resulting models. These cases are representative, as similar results are found for other profiles with a similar shape. While the Ca II 8542 Å line is sensitive up to approximately $\log\tau = -5.8$ in the quiet Sun, with peak sensitivity around $\log\tau = -5.2$, its upper optical depth with significant sensitivity extends only to about $\log\tau = -3.8$ during the flare, after which it rapidly decreases. This important change in optical depth must be considered when analyzing the LOS velocity maps.

Given that the RF during the flare peaks at approximately $\log\tau = -3.5$, we chose to present the LOS velocities inferred with STiC at $\log\tau = -2.0$, -2.5, and -3.5 in Fig. 3. Outside this range, the sensitivity of the Ca II line to Doppler velocities quickly drops. After several tests, two different inversion strategies were used to retrieve the Doppler velocities (see Table 1). Focusing on the flaring area of Fig. 3, the velocities in the upper row (configuration A) change smoothly from the lower atmospheric layers ($\log\tau = -2.0$) to the higher layers ($\log\tau = -3.5$). In contrast, in the lower panels (configuration B) there is an abrupt change in the sign of the velocities between $\log\tau = -2.5$ and -3.5. To understand this difference, a few individual example profiles (pixels a–d in Fig. 1f), and their fit from the inversions, are shown in Fig. 4. The pixels belong to the front of the flare ribbon. The observed profiles appear as black dots, whereas the best fit from the inversions is overplotted as solid orange and pink lines, for the inversions with configuration A and B, respectively. Critically, the two models reproduce the observations with comparable precision, indicating the degeneracy of the inversion process. Specifically, while the models show similar redshifts at the lower and middle layers ($\log\tau = -2$ and -2.5) where a strong red-wing asymmetry is observed around 8542.6 Å, their solutions differ significantly in the higher layers (above $\log\tau = -3.0$). In these higher layers, where the line core is formed, the pink model systematically shows blueshifts, while the orange model exhibits redshifts. The reason why the inversion code converges to two distinct solutions can be

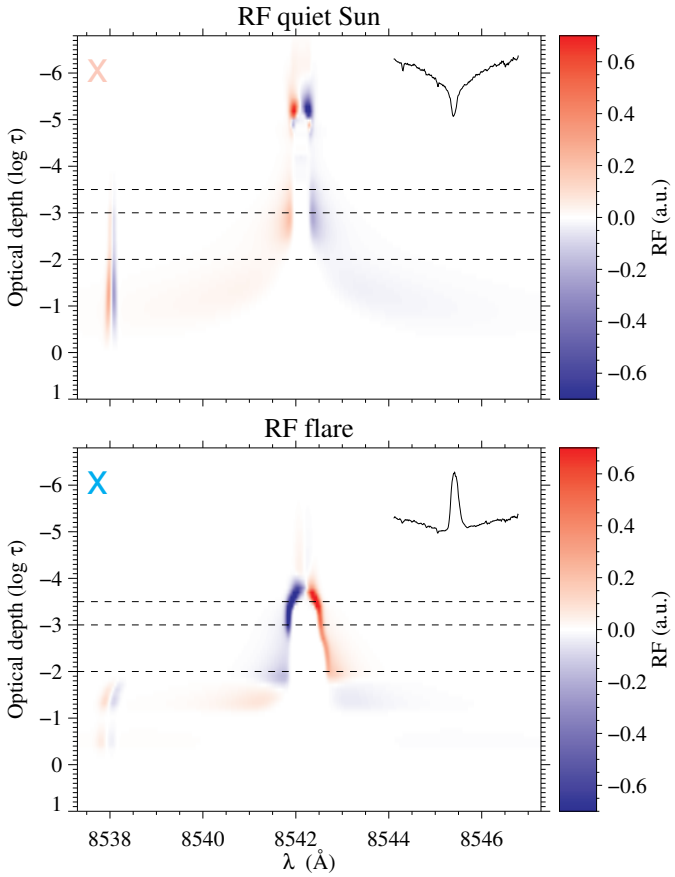

Fig. 2. Response functions of the Ca II 8542 Å spectral line to changes in the LOS velocity. The lower panel corresponds to a pixel within the bright flare, at the ribbon front at coordinates $x, y = 33\farcs9, 44\farcs6$ (see light blue cross in Fig. 1f), whereas the upper panel shows the RF in a quiet-Sun pixel (pink cross in Fig. 1f at $x, y = 35\farcs0, 75\farcs2$). The RFs are normalized to their maximum absolute value and saturated between ±0.7 to enhance the weaker areas. The corresponding observed intensity profile is shown in the upper right corner of each panel and extends over the same spectral range as the RF. The horizontal dashed lines mark the optical depths at $\log\tau = -2.0$, -3.0, and -3.5.

attributed to the flexibility inherent in configuration B, which has more freedom during the first inversion cycle compared to configuration A. These results show that the red asymmetry near the line core can be explained by two possible scenarios: a redshifted emission (configuration A) or a blueshifted absorption (configuration B). To determine which scenario is more physically plausible and to understand the velocity structure in these upper layers, we analyzed the He I LOS velocities, and the results are presented below.

4.2. He I 10830 Å

The LOS velocities inferred from the He I triplet during the flare (map 2, Fig. 1b) are displayed in the upper panel of Fig. 5. The solid and dotted crosses in the upper panel mark the positions of the spectral profiles shown in the lower panel. The He I triplet appears to be broadened, clearly redshifted, and strongly in emission. The gray line shows the quiet-Sun profile, while the red line shows the fit to the flare profile retrieved from the HAZEL inversions. The fits are accurate, and the obtained velocities within the flaring area are dominated by redshifts.

Interestingly, surrounding the redshifted flare area, at the front of the flare ribbons, the velocities are blueshifted. After inspection of the spectral profiles (discussed in Sect. 5.2), we conclude that these blueshifts are real, as the profiles exhibit a blueshifted absorption component that co-exists with another, weaker, emission component. Two-component spectral inversions would be necessary to fit this redshifted emission profile. The co-existence of blue- and redshifted He I profiles is interesting in itself and shows that this phenomenon is common in pixels affected by the leading edge of the flare. We come back to this in the discussion.

4.3. Ambiguity in the velocities during the peak

The ambiguity seen in the Ca II 8542 Å velocities of Fig. 3 can be solved by comparing them to the He I 10830 Å velocities in Fig. 5. The main bright flaring area, which is dominated by emission profiles, is uniformly redshifted for the He I velocities, apart from the narrow region at the ribbon front. Since He I forms higher in the atmosphere, a solution where Ca II is also redshifted seems more plausible. In addition, a visual inspection of the example profiles in Fig. 4 reveals shifts of the line core toward the red. Therefore, configuration A from Table 1 of the Ca II inversions is strongly favored. The results must therefore be interpreted with caution, ideally using a second spectral line in the chromosphere if available, as in the present study. Another interpretation, although inconsistent with our discussion, is based on the inversion code's results from configuration B, which identify the lower-lying left wing of the Ca II 8542 Å line (see Fig. 4) as a blueshifted absorption profile. For the remainder of this study, we present only the Ca II LOS velocities obtained from the simpler inversions using configuration A of Table 1.

4.4. Temporal evolution

The LOS velocities for the different phases of the M-class flare are exhibited in Fig. 6. The upper panels show the velocities retrieved from the He I inversions, whereas the middle and lower panels show the velocities inferred from the Ca II inversions at $\log\tau = -3.5$ and -2.0. For a better comparison in time, we focus on the black rectangles, which show the common FOV across the four maps. The pre-flare map shows the blueshifts associated with the central filament in the upper He I panel. These upflows, although much weaker, are also seen in the Ca II at the $\log\tau = -3.5$ layer. Surrounding the filament we mainly see redshifts.

The second column in Fig. 6 illustrates the LOS velocities during the M3.2 flare. Within the black box, we see downflows in the central part, which belong to the main flare ribbon, among all layers. These redshifts are linked to the largest emission profiles of He I and Ca II. Interestingly, a narrow area at the front of the flare ribbon, also called the leading edge of the flare, shows blueshifts. This is nicely seen in the He I velocity map, and is less pronounced but consistent, in some parts of the Ca II velocity maps. The He I velocities at this blueshifted thin layer are between -4 and $-10\,\mathrm{km\,s^{-1}}$. The Ca II velocities at $\log\tau = -3.5$ also show a well-enhanced patch of blueshifts at the upper right leading flaring front at about $(x, y = 47'', 44'')$. The velocities are between -2 and $-5\,\mathrm{km\,s^{-1}}$, and much lower (about $-1\,\mathrm{km\,s^{-1}}$) at $\log\tau = -2.0$. The small southern ribbon $(x, y = 25'', 15'')$ exhibits mostly blueshifts in He I and Ca II at $\log\tau = -2.0$, whereas Ca II at $\log\tau = -3.5$ shows blueshifts only at the southern edge of that ribbon.

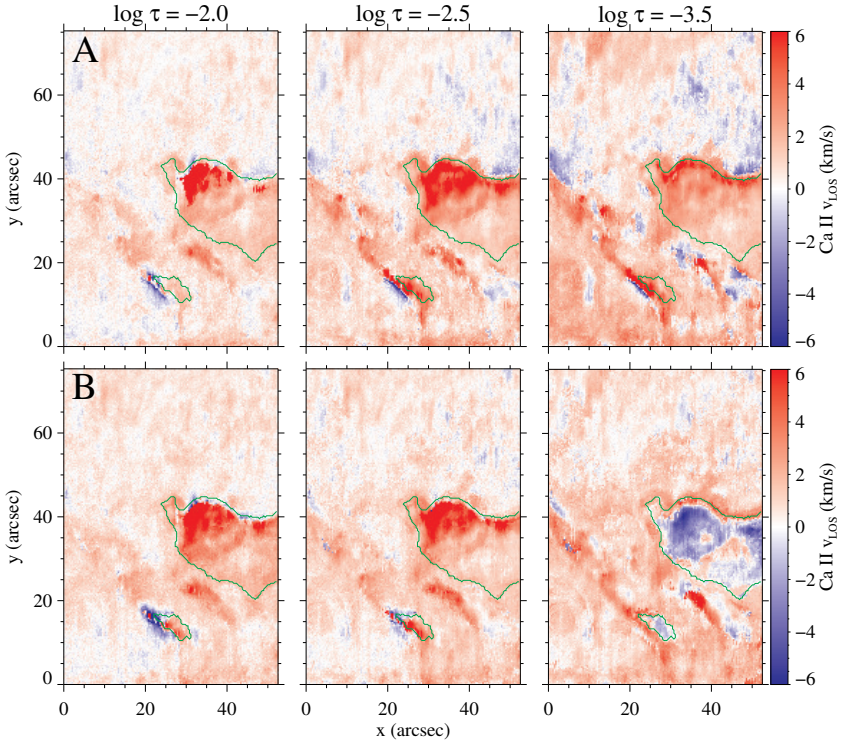

Fig. 3. Comparison of the Ca II 8542 Å LOS velocities at different optical depths, using two different inversion strategies with STiC (see Table 1) during the M-class flare (map 2 or panel f) in Fig. 1). Top (A): Restrictions applied to the inversion code. Bottom (B): Solution leaving the code with more freedom. The velocities are clipped between $\pm 6\,\mathrm{km\,s^{-1}}$. The faint green contours mark the borders of the ribbons as seen in Fig. 1f), using an intensity threshold at $I/I_c = 0.87$.

The filament partially remains blueshifted, with larger parts redshifted in Ca II. No eruption of the filament takes place at any time. The redshifted flare front of the large central ribbon, next to the leading blueshifted edge, shows LOS velocities in He I in the range of $10-13\,\mathrm{km\,s^{-1}}$. LOS velocities between $5-9\,\mathrm{km\,s^{-1}}$ are found in the upper ribbon at the flare front for Ca II at $\log\tau = -3.5$, whereas at $\log\tau = -2.0$ the velocities are even larger, between $10-25\,\mathrm{km\,s^{-1}}$. The central part of the ribbon (around $x, y \sim 35'', 38''$) exhibits slower velocities, in the range of $2-7\,\mathrm{km\,s^{-1}}$ for He I and Ca II at $\log\tau = -2.0$, and $2-5\,\mathrm{km\,s^{-1}}$ at $\log\tau = -3.5$.

The last two post-flare maps display extensive downflows on both sides of the filament, featuring redshifted profiles. These downflows occur at the footpoints of a loop system that crosses the filament and the PIL, as shown in a magnetogram by Kuckein et al. (2015b), with its roots in different polarities. The loop system is clearly seen in the He I maps in Fig. 1 (panels c–d). The redshifts are most prominent in He I on both sides of the filament. In the Ca II velocities, the southern side exhibits much stronger redshifts, while the upper part shows only minor shifts at $\log\tau = -2.0$. Although the He I maps suggest that plasma flows consistently downward on both sides of the filament, the Ca II maps indicate a clear preference for the southern side. The He I velocities in the southern footpoint are between $20-30\,\mathrm{km\,s^{-1}}$, whereas the upper footpoint has areas of up to $39\,\mathrm{km\,s^{-1}}$, in the first post-flare map. In the second post-flare map, the area of strong redshifts decreases, though some pixels of about $30\,\mathrm{km\,s^{-1}}$ still exist in both footpoints. The Ca II post-flare maps exhibit downflows in the southern footpoints. At $\log\tau = -3.5$, only a small patch is visible, which appeared shortly after the flare at approximately $(x, y) \sim (22'', 27'')$, with LOS velocities in the range of $6-10\,\mathrm{km\,s^{-1}}$. In the second post-flare map the patch had vanished. The lowest atmospheric layer, given by $\log\tau = -2.0$ of the Ca II line, shows similar flows in the southern footpoint, in the range of $7-9\,\mathrm{km\,s^{-1}}$ with peaks slightly exceeding $10\,\mathrm{km\,s^{-1}}$ for the first post-flare map. In the second post-flare map, the velocities have weakened considerably, and both footpoints exhibit redshifted LOS velocities of about $3-5\,\mathrm{km\,s^{-1}}$ with peaks of $\sim 6\,\mathrm{km\,s^{-1}}$ in the northern footpoint.

5. Discussion

5.1. Height sensitivity of the Ca II line

The computed response functions for Ca II 8542 Å in the flare ribbon indicate a shift in spectral line sensitivity to Doppler shifts toward lower heights (Fig. 2). This affects the interpretation of the results, as the Ca II line core is typically expected to form higher in the atmosphere.

Kuridze et al. (2018) computed RFs for Ca II in response to temperature and LOS magnetic-field changes in an M-class flare. Consistent with our M3.2 flare results, they found an optical depth shift to lower heights, closer to the photosphere during the flare. This effect is also observed, but less prominent, in smaller flares. Yadav et al. (2021) demonstrated in their Fig. 11 that, in a C2 flare, the Ca II line wings become sensitive down to $\log\tau \sim -2$, while the line core shifts down by approximately $\Delta\log\tau \sim 0.5$ in optical depth.

All the above-mentioned studies, including ours, consistently show a decrease in the height of Ca II line sensitivity. Kerr et al. (2016) found the same behavior in simulations, attributing it to high temperatures that reduce the upper-level population of Ca II 8542 Å, shifting the formation height downward. We emphasize that Ca II is ionized to Ca III, making it undetectable in the Ca II 8542 Å observations. This implies that the analysis should be restricted to greater optical depths (Fig. 2), that is lower heights, than is typically done in active-region studies with this spectral line. It is also worth noting that a downward shift in the height of line sensitivity has also been observed in other spectral lines during flares. In particular, the He I 10830 Å

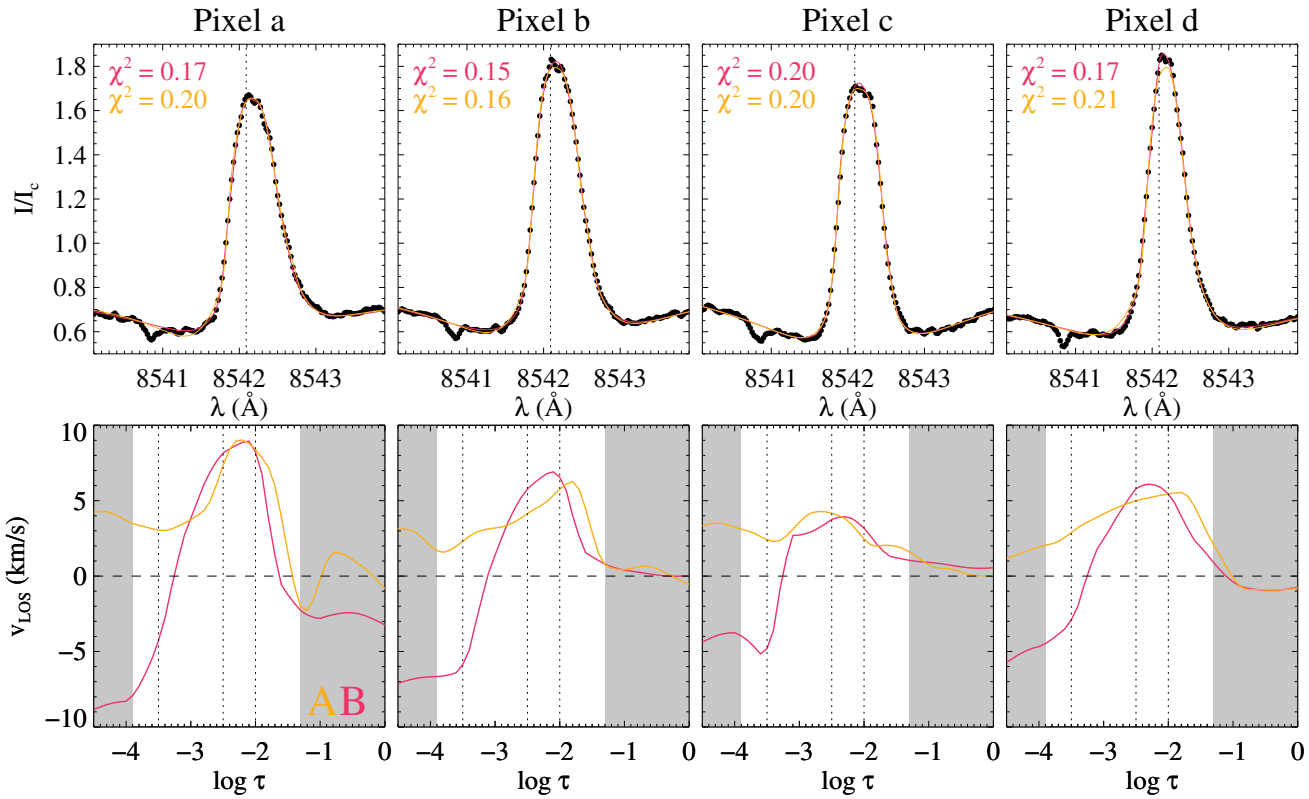

Fig. 4. Selected Ca II 8542 Å profiles from the flare-front ribbon and inferred LOS velocity stratification. Top: Observed Ca II intensity profiles (black dots); fit from the inversions using two different inversion configurations (pink and orange lines; Table 1). The χ^2-test shows similar values for both fits. The vertical dotted line marks the center of the Ca II line at rest. Bottom: Inferred LOS velocity stratification with height on an optical depth scale. The orange (pink) line corresponds to configuration A (B) of the inversion (see Table 1). The vertical dotted lines mark the three optical depths shown in Fig. 3. The position of the pixels within the FOV is represented in panel f) of Fig. 1. The velocities shown inside the shaded area are not trustworthy, as the RF is very low in that area.

and He I D_3 lines can exhibit a similar behavior (Anan et al. 2018; Libbrecht et al. 2019).

5.2. Leading front of the flare

The present M3.2 flare observations reveal a leading front of the ribbon dominated by chromospheric blueshifts. This is most prominent in the He I 10830 Å velocity map during the flare (Fig. 6) and remains visible, though less pronounced, in the first (lower left area) and second post-flare maps. The Ca II 8542 Å velocity maps also exhibit this behavior, but the response is weaker, with less prominent blueshifts. Next to the leading edge of the flare, the bright part with clearly redshifted emission profiles follows. The blueshifted flare front in the He I observations stems from the presence of two distinct velocity components within each pixel, one blueshifted and one redshifted; our inversions predominantly favor the blueshifted component. Figure 7 exhibits four example profiles of He I 10830 Å from the leading front, surrounding the bright flare area. Although pixel δ is mostly redshifted, there is also a shallow blueshifted He I profile, which the inversion code did not fit. During the inversion process of the spectral profiles, the inversion code mostly favored the blueshifted profile, producing a homogeneous blueshifted area in space surrounding the bright redshifted emission profiles (Figs. 6 or 5). The coexistence of two components may indicate that two mechanisms of line formation are at work, or even the transition from one mechanism to the other due to the flare. On the one hand, the triplet can be populated by increased extreme ultraviolet (EUV) photoionization due to the flare and subsequent recombinations (Mauas et al. 2005; Centeno et al. 2008). On the other hand, nonthermal collisional ionization and recombination can generate He I (Ding et al. 2005). It seems reasonable that both mechanisms are enhanced during flares when there is evidence for nonthermal electrons in the chromosphere. Kerr et al. (2021) found that the latter mechanism was necessary to produce flare-induced dimming of He I 10 830 Å. We likely see this dimming only at the north front of the flare ribbon in Fig. 1b, which is typically seen as a darkening in He I line-core images. Xu et al. (2016) also reported dimmings on only one side of the flare ribbon. The reason for not seeing it clearly in our observations might be the lack of spatial resolution needed to identify these dimmings of about 340 km (~0.″47), as reported by Xu et al. (2016). Our theoretical spatial resolution is ~0.″70. Nevertheless, dimming is produced by having He I absorption profiles, which we found shifted to the blue in the flare front (e.g., pixels α and β in Fig. 7). The lifetime of the dimming is about 91 s (Xu et al. 2016). Our data does not have sufficient time resolution to measure the duration of our dimming; the raster scan took about 30 min. However, the presence of blueshifted absorption profiles alongside emission profiles within the same pixel suggests a rapid transition to redshifted emission profiles in the bright area as the flare evolves.

A blueshifted flare front has been reported in other chromospheric lines (Panos et al. 2018). Polito et al. (2023) reported Mg II k3 blueshifts at the leading edge of an X-class flare (their Fig. 4). Moreover, the authors found that the optically thin

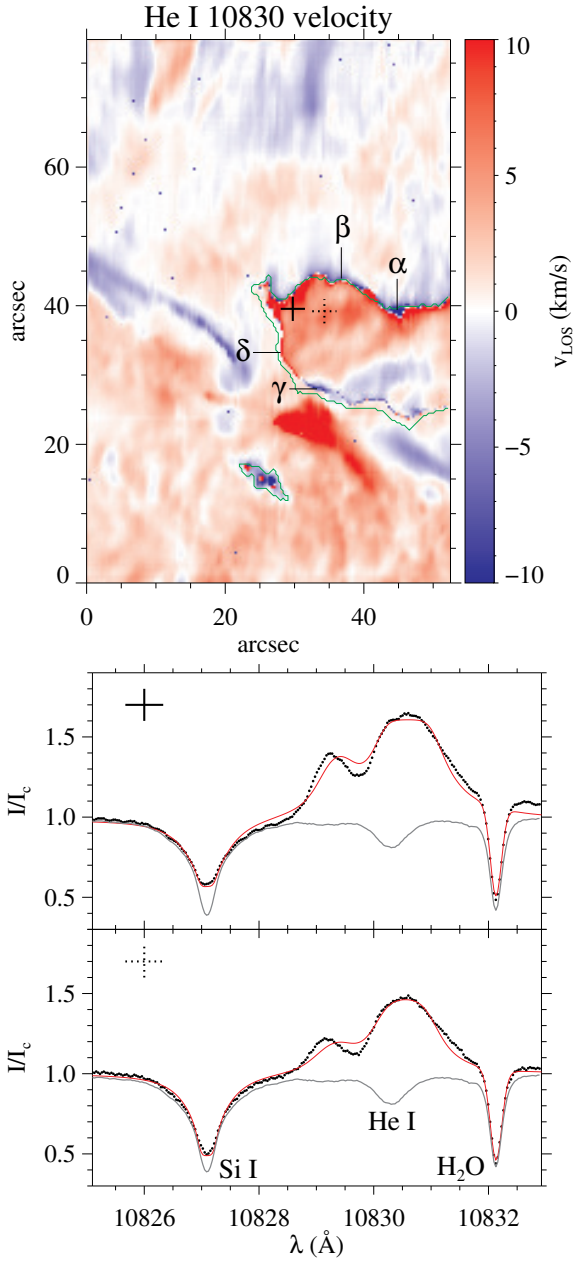

Fig. 5. Top: Slit-reconstructed LOS velocity map of the flare inferred from the He I 10830 Å inversions using HAZEL. The map is clipped between $\pm 10\,\mathrm{km\,s^{-1}}$. Flows directed away (toward) the observer are shown in red (blue; see color bar at right). The faint green contour marks the borders of the ribbons, as seen in Fig. 1b), using an intensity threshold at $I/I_c = 0.87$. Bottom: Two example intensity profiles observed within the flaring area. The black dots are the observations, whereas the red solid line depicts the fit from the HAZEL inversion. The two profiles are marked in the velocity map (top panel) with a solid and a dotted cross; the profiles correspond to an inferred velocity of 8.0 and $6.9\,\mathrm{km\,s^{-1}}$, respectively, retrieved from the He I fit. The solid gray line shows the average quiet-Sun profile. The letters $\alpha-\gamma$ show the positions of the leading-edge profiles exhibited in Fig. 7.

transition region line O IV was also blueshifted in some locations of the flare front. Tei et al. (2018) showed Mg II blueshifted lines of about $-10\,\mathrm{km\,s^{-1}}$, which evolved into redshifts at the flare front of a C5.4 flare. The authors propose a cool-upflow scenario (their Fig. 12) to explain this phenomenon: high-energy electrons reach deeper layers, heating the plasma to temperatures on the order of 10^6 K. As a result, the cooler chromospheric plasma above the heated region is pushed upward, appearing briefly as a blueshift in chromospheric spectral lines until the intense radiation from the condensation region dominates. Although our data lack the temporal resolution needed to follow the evolution of the profiles, we find blue and redshifted profiles within the same pixel, indicating that a very short time may pass in the transition from blue- to redshifted profiles. The lifetime of the blueshifted Mg II profiles presented by Tei et al. (2018) is, on average, 29 s.

Numerical experiments on the ribbon front in flares support the scenario of high-energy electrons penetrating deeper layers, primarily perturbing the mid-chromosphere (Kerr et al. 2024). Evaporation then takes place producing upflowing plasma, the blueshifted leading edge. At some point the upper chromosphere is strongly affected by the flare and the plasma flows become redshifted, producing the emission areas seen in He I and Ca II (Fig. 1). This explains why our Ca II velocities exhibit much weaker blueshifts at the ribbon front (Fig. 6) because the line is formed deeper in the atmosphere than He I.

Our He I 10 830 Å data reveal a blueshifted leading front, a feature whose interpretation remains open in the context of our event. It could be attributed either to rapid chromospheric heating (Tei et al. 2018) or to gentle evaporation (Kerr et al. 2024). A detailed thermal analysis could help clarify this question, but it is deferred to a future study, as it is beyond the scope of the present work.

5.3. Ca II 8542 Å line shape and shifts

It is worth discussing the shape of the Ca II 8542 Å line during the flare. The current data show the line at a much finer spectral sampling (25 mÅ) compared to flare studies based on imaging-spectroscopy instruments. Figure 4 shows an example of four intensity profiles selected close to the front of the flare ribbon. They show clear emission profiles without a central reversal of the line core (as shown in the simulations (Kerr et al. 2016)) and with peaks of about $I/I_c \sim 1.7$. In contrast, Kuridze et al. (2018) showed in their Fig. 6 averaged Ca II 8542 Å flare profiles with a shallow dip in the line-core center, in an M1.9 flare. Moreover, Kuridze et al. (2017) reported a weaker emission profile, without central reversal, in a C8.4 flare. Ferrente et al. (2024) showcased two Ca II profiles inside the flare ribbon of an X-class flare. One profile reaches a peak of about $I/I_c \sim 2.0$, without a central reversal. Rubio da Costa et al. (2016) also presented Ca II profiles in their Fig. 3 during an X-class flare, showing no central reversal in the flare ribbon. Our profiles seem compatible, but show more details in the core and wings due to the better spectral resolution. All profiles from the flare front shown in Fig. 4 have an asymmetric shape, with a predominant broader red wing indicating velocity gradients and downward plasma motions. Interestingly, the peak intensity is not at the center of the core of the line. Kerr et al. (2016) found in their simulations of the Ca II 8542 Å line during flare heating a tiny shifted component in the core. They interpreted it as optically thin emission with a higher temperature than the rest of the core. Nevertheless, because the line is optically thick, its peak intensity does not necessarily correspond to the core of the line. In Fig. 4, the small optically thin emission within the core is always found toward the blue. However, the inversion code can hardly account for these tiny shifts inside the core. Therefore, the impact on the inversions seems rather negligible. We note that the flare profiles from an M1.1 flare shown by Kuridze et al. (2015) in their Fig. 3 might also indicate a slightly blueshifted peak inside the core of

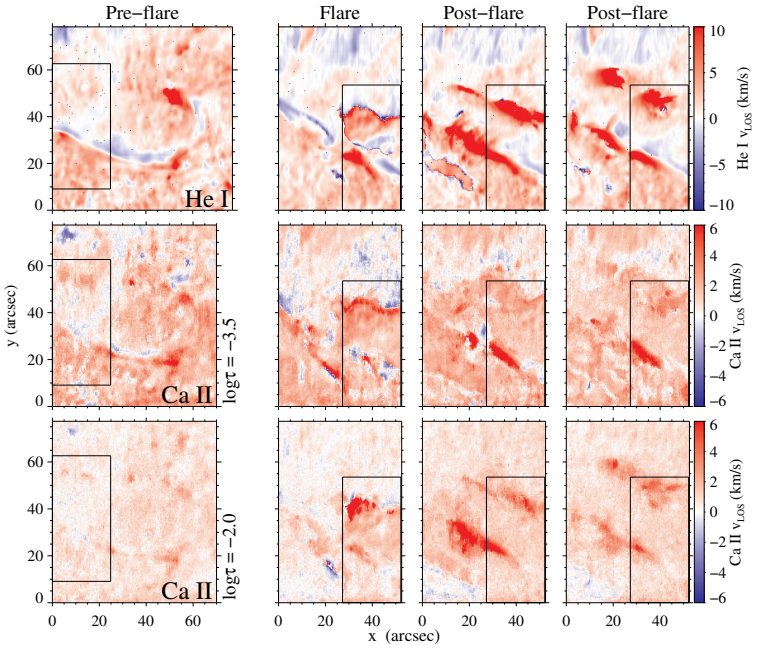

Fig. 6. LOS velocities at different times of the flare inferred from the inversions. From top to bottom: He I 10830 Å, Ca II 8542 Å at $\log\tau = -3.5$, and $\log\tau = -2.0$. The first column of velocity maps corresponds to the pre-flare phase (07:49–08:29 UT). The second column shows the peak of the flare (08:35–09:05 UT). The third and fourth columns depict the post-flare phases corresponding to the time ranges (09:07–09:36 UT) and (09:38–10:08 UT), respectively. We note that the top panels corresponding to the He I LOS velocities are clipped between $\pm 10\,\mathrm{km\,s^{-1}}$, whereas the middle and lower panels of Ca II LOS velocities are saturated between $\pm 6\,\mathrm{km\,s^{-1}}$. The black box shows the common FOV among all raster scans.

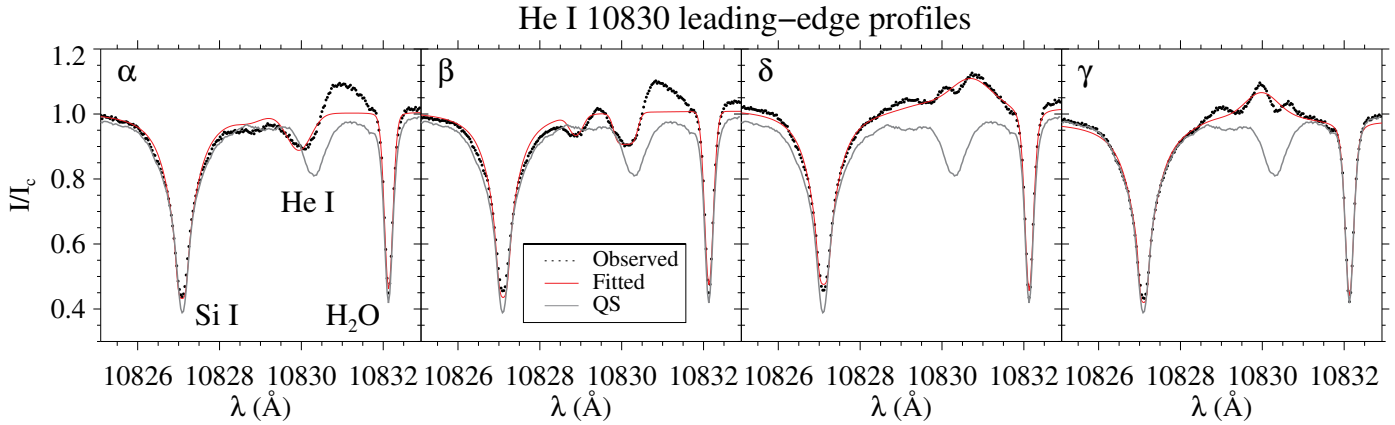

Fig. 7. Examples of He I 10830 Å intensity profiles found at the leading front of the flare ribbon. The dots represent the observed profiles and the red solid line is the fit from the HAZEL inversions. The quiet-Sun profile, which is at rest, is shown in gray to better identify the Doppler shifts. The positions of the four profiles (α, β, δ, and γ) appear in Fig. 5; the inferred velocities are −10.0, −5.8, 10.9, and $-9.1\,\mathrm{km\,s^{-1}}$, respectively. In panel α, the absorption seen in He I is the blueshifted component, whereas the He I emission profile is the redshifted component.

the line. Nevertheless, their spectral sampling is much too broad (100 mÅ) to confirm this peak reliably.

5.4. Plasma-flow and flare-loop evolution during the flare

Figure 6 shows the evolution of the LOS velocities at different stages of the flare and at several heights. It is worth keeping Fig. 1 in mind to compare the velocities to their intensity raster scans. The impulsive phase of the flare (second column in Fig. 6) leaves an important imprint in the chromosphere. Not only do the He I 10830 Å and Ca II 8542 Å profiles appear in emission (e.g., Figs. 4, 5, and 7), but most of these profiles are also redshifted. Hence, we see plasma flows toward the solar surface in the heated part and across all layers. We note a faint blueshifted region ($x, y \sim 40'', 30''$) in the He I velocity panels in Fig. 6, located within the central flare ribbon and inside the black square. This flow remains spatially and temporally persistent in the subsequent post-flare maps. Therefore, it seems not to be part of the flare ribbon itself, which moves away from the PIL, but could show long-lasting slow evaporation.

Although redshifts dominate the flare ribbon in our data, a recent study of an X-class flare by Ferrente et al. (2024) reports predominantly blueshifts all over the ribbon at $\log\tau = -4$ with velocities of about $-20\,\mathrm{km\,s^{-1}}$. We raise the question of whether the strong upflows at $\log\tau = -4$ could result from ambiguous solutions in the inversion code, similar to those discussed in Sect. 4.3. These upflows represent a well-defined solution to the fitting problem, particularly given the significant sensitivity of the RF at that layer in their study. In our case, an examination of the spectral profiles revealed that not only do the flare-emission profiles exhibit a red asymmetry, but the inner core of the line is also shifted toward the red. We speculate that with fewer spectral points, as in their observations, the inversion code might be more likely to find alternative solutions for the same profiles. Notably, identifying different solutions requires running the computationally intensive inversion process multiple times. This question has been raised before; since the 1980s, researchers have reported observations of areas within ribbons with strong red-asymmetries, suggesting that these features are more likely due to the downward motion produced by the impulsive heating

than attenuation in the blue wing due to rising matter over the flare (Ichimoto & Kurokawa 1984). This highlights the importance of multiple chromospheric lines in resolving such ambiguities, as in the present study, and new diagnostic tools that can capture the multi-modality of the solution (Díaz Baso et al. 2022).

In addition, as highlighted in Sect. 5.2, a blueshifted leading edge of the flare ribbon is seen more prominently in the He I velocities. We assume that chromospheric evaporation, as described by Tei et al. (2018) and Kerr et al. (2024), is the reason for these short-lived blueshifts. Blueshifts are predominantly observed at the northern edge of the flare ribbon, consistent with previous studies that have reported enhanced absorption in only one flare ribbon.

Following the ionization of He I 10830 Å due to the flare, recombination sets in, producing strong absorption in the flare-affected region. The first post-flare velocity map (column 3 in Fig. 6) of He I 10830 Å reveals strong downflows on both sides of the filament, and hence the PIL. The intensity raster scan reveals dense He I absorption following loop-like arches crossing the filament, connecting opposite polarities. Interestingly, the loop tops do not exhibit significant velocities, suggesting that these loops are predominantly at rest and are not expanding at this stage of the flare (about 30 min after the impulsive phase). The plasma flows at the footpoints of the loops are strongly enhanced, suggesting plasma flowing downward following these loops. Notably, Ca II 8542 Å does not display loop-like structures in Fig. 1, likely because most Ca II is ionized at the higher loop-top regions. The strongest downflows appear at the footpoints of the loops in both polarities for He I, whereas Ca II exhibits strong redshifts only on one side of the PIL at $\log\tau = -3.5$. These downflows at the footpoints persist; they are also observed in the one-hour-later post-flare velocity map for both He I and Ca II at $\log\tau = -2.0$.

A persistent strong redshifted area, of about 10 km s^{-1}, draws our attention to the lower left part within the black box in Fig. 6, at all stages of the flare, and across all shown heights ($x, y \sim 30'', 23''$). This area is outside of the flare ribbon. The redshifts start at the impulsive phase of the flare, but less pronounced in Ca II compared to He I, and are present for at least one hour. The raster scans in Fig. 1 indicate that the redshifts are close to the filament. We therefore speculate that these redshifts are related to the filament, which remains stable during the flare. The literature also contains examples of active region filaments that persist after a flare occurs over them (e.g., Díaz Baso et al. 2019b), emphasizing the importance of magnetic connectivity during the evolution of these events.

6. Summary and conclusions

We presented the chromospheric LOS velocities associated with an M3.2 flare, as inferred from the combined analysis of two different spectral regions: the He I 10830 Å triplet and the Ca II 8542 Å line. The ground-based raster observations at VTT covered the pre-flare, flare, and post-flare phases.

Our main findings are the following:

1. The response function analysis reveals that the Ca II 8542 Å line forms at lower heights during flares, with peak sensitivity shifting from $\log\tau \approx -5.2$ to -3.5 in our M3.2 flare. These results are consistent with the limited studies that have investigated Ca II RFs in other flare classes.
2. Using multiple chromospheric spectral lines is crucial for resolving inversion ambiguities in the LOS velocities, as demonstrated by our comparison between He I and Ca II velocities (Sect. 4.3).
3. The flare exhibits blueshifts at the narrow leading edge of the ribbons, best seen at He I 10 830 Å with LOS velocities of up to -10 km s^{-1}, and redshifts in the main bright flaring areas across all spectral lines with velocities between 2–13 km s^{-1} in He I. The blueshifted leading-edge profiles mostly reveal a coexistence of blueshifted absorption and redshifted emission components in He I 10830 Å (see Fig. 7). This supports a cool-upflow scenario with rapid transition from upflows to downflows, likely occurring within seconds to tens of seconds.
4. Dimming in He I is likely seen on only one side of the flare ribbon, similar to the few other He I observations during flares.
5. Post-flare observations show loop-like structures in He I connecting opposite polarities with strong downflows at footpoints (up to 39 km s^{-1}), while Ca II exhibits asymmetric downflows that are much stronger in the southern footpoint. The Ca II downflows are up to 10 km s^{-1} for both $\log\tau = -3.5$ and $\log\tau = -2.0$. No loop-like structures are seen in Ca II.
6. The filament remained stable throughout the flare, and showed no signs of eruption.

This study demonstrates the importance of combining spectroscopic observations from different chromospheric lines to create a comprehensive picture of flare dynamics. This is particularly important for understanding the complex velocity fields during different phases of solar flares. Additional high-resolution multi-wavelength observations are crucial to further understanding the chromospheric dynamics during flares. The advent of new-generation solar telescopes such as DKIST (Rimmele et al. 2020), EST (Quintero Noda et al. 2022), and WeHot (Song et al. 2024) will be crucial in this regard.

Acknowledgements. The Vacuum Tower Telescope is operated by the Institute for Solar Physics in Freiburg, Germany, at the Spanish Observatorio del Teide, Tenerife, Canary Islands. This project has received funding from the European Union's Horizon 2020 research and innovation programme under the Marie Skłodowska-Curie grant agreement No 895955. We acknowledge support from the Agencia Estatal de Investigación del Ministerio de Ciencia, Innovación y Universidades (MCIU/AEI) under grant "Polarimetric Inference of Magnetic Fields", the European Regional Development Fund (ERDF) with reference PID2022-136563NB-I00/10.13039/501100011033. CK acknowledges grant RYC2022-037660-I funded by MCIN/AEI/10.13039/501100011033 and by "ESF Investing in your future". MC acknowledges financial support from Ministerio de Ciencia e Innovacion and the European Regional Development Fund through grant PID2021-127487NB-I00. This research is supported by the Research Council of Norway, project number 325491, and through its Centres of Excellence scheme, project number 262622. TF acknowledges grants PID2021-127487NB-I00, CNS2023-145233 and RYC2020-030307-I funded by MCIN/AEI/10.13039/501100011033. CQN acknowledges Project ICTS2022-007828, funded by MICIN and the European Union NextGeneration EU/RTRP. LK acknowledges support from an SNSF PRIMA grant and a SERI-funded ERC CoG grant. LF acknowledges support from UK Research and Innovation's Science and Technology Facilities Council grant ST/X000990/1. SM acknowledges support from STFC grants ST/W001004/1 and ST/V003658/1. Drs. H. Socas-Navarro, B. Ruiz Cobo, and E. S. Carlin are greatly acknowledged for fruitful discussions.

References

Anan, T., Yoneya, T., Ichimoto, K., et al. 2018, PASJ, 70, 101
Asensio Ramos, A., Trujillo Bueno, J., & Landi Degl'Innocenti, E. 2008, ApJ, 683, 542
Avrett, E., Fontenla, J., & Loeser, R. 1994, IAU Symp., 154, 35
Berkefeld, T., Soltau, D., Schmidt, D., & von der Lühe, O. 2010, Appl. Opt., 49, G155

Centeno, R., Trujillo Bueno, J., Uitenbroek, H., & Collados, M. 2008, ApJ, 677, 742
Collados, M. 1999, ASP Conf. Ser., 184, 3
Collados, M. V. 2003, SPIE Conf. Ser., 4843, 55
Collados, M., Lagg, A., Díaz García, J. J., et al. 2007, ASP Conf. Ser., 368, 611
Cox, A. N. 2000, Allen's astrophysical quantities, 700
de la Cruz Rodríguez, J., Leenaarts, J., Danilovic, S., & Uitenbroek, H. 2019, A&A, 623, A74
Díaz Baso, C. J., Martínez González, M. J., Asensio Ramos, A., & de la Cruz Rodríguez, J. 2019a, A&A, 623, A178
Díaz Baso, C. J., Martínez González, M. J., & Asensio Ramos, A. 2019b, A&A, 625, A128
Díaz Baso, C. J., de la Cruz Rodríguez, J., & Leenaarts, J. 2021, A&A, 647, A188
Díaz Baso, C. J., Asensio Ramos, A., & de la Cruz Rodríguez, J. 2022, A&A, 659, A165
Ding, M. D., Li, H., & Fang, C. 2005, A&A, 432, 699
Ferrente, F., Zuccarello, F., Guglielmino, S. L., Criscuoli, S., & Romano, P. 2023, ApJ, 954, 185
Ferrente, F., Quintero Noda, C., Zuccarello, F., & Guglielmino, S. L. 2024, A&A, 686, A244
Fisher, G. H., Canfield, R. C., & McClymont, A. N. 1985, ApJ, 289, 425
Fletcher, L., Dennis, B. R., Hudson, H. S., et al. 2011, Space Sci. Rev., 159, 19
Fontenla, J. M., Avrett, E. H., & Loeser, R. 1993, ApJ, 406, 319
Harvey, J. W. 2012, Sol. Phys., 280, 69
Hudson, H. S. 2007, ASP Conf. Ser., 368, 365
Ichimoto, K., & Kurokawa, H. 1984, Sol. Phys., 93, 105
Judge, P. G. 2015, ApJ, 808, 116
Kerr, G. S., Fletcher, L., Russell, A. J. B., & Allred, J. C. 2016, ApJ, 827, 101
Kerr, G. S., Xu, Y., Allred, J. C., et al. 2021, ApJ, 912, 153
Kerr, G. S., Polito, V., Xu, Y., & Allred, J. C. 2024, ApJ, 970, 21
Keys, P. H., Jess, D. B., Mathioudakis, M., & Keenan, F. P. 2011, A&A, 529, A127
Kleint, L. 2012, ApJ, 748, 138
Kleint, L. 2017, ApJ, 834, 26
Kleint, L., Heinzel, P., Judge, P., & Krucker, S. 2016, ApJ, 816, 88
Kuckein, C., Martínez Pillet, V., & Centeno, R. 2012, A&A, 542, A112
Kuckein, C., Collados, M., & Manso Sainz, R. 2015a, ApJ, 799, L25
Kuckein, C., Collados, M., Sainz, R. M., & Ramos, A. A. 2015b, IAU Symp., 305, 73
Kuckein, C., Diercke, A., González Manrique, S. J., et al. 2017, A&A, 608, A117
Kuridze, D., Mathioudakis, M., Simões, P. J. A., et al. 2015, ApJ, 813, 125
Kuridze, D., Henriques, V., Mathioudakis, M., et al. 2017, ApJ, 846, 9
Kuridze, D., Henriques, V. M. J., Mathioudakis, M., et al. 2018, ApJ, 860, 10
Libbrecht, T., de la Cruz Rodríguez, J., Danilovic, S., Leenaarts, J., & Pazira, H. 2019, A&A, 621, A35
Martínez Pillet, V., Lites, B. W., & Skumanich, A. 1997, ApJ, 474, 810
Mauas, P. J. D., Andretta, V., Falchi, A., et al. 2005, ApJ, 619, 604
Milligan, R. O. 2015, Sol. Phys., 290, 3399
Milligan, R. O., Kerr, G. S., Dennis, B. R., et al. 2014, ApJ, 793, 70
Moore, C. E., Minnaert, M. G. J., & Houtgast, J. 1966, The solar spectrum 2935 A to 8770 A (Washington: US Government Printing Office)
Neckel, H., & Labs, D. 1984, Sol. Phys., 90, 205
Panos, B., Kleint, L., Huwyler, C., et al. 2018, ApJ, 861, 62
Penn, M. J., & Kuhn, J. R. 1995, ApJ, 441, L51
Polito, V., Kerr, G. S., Xu, Y., Sadykov, V. M., & Lorincik, J. 2023, ApJ, 944, 104
Priest, E. R., & Forbes, T. G. 2002, A&ARv, 10, 313
Quintero Noda, C., Shimizu, T., de la Cruz Rodríguez, J., et al. 2016, MNRAS, 459, 3363
Quintero Noda, C., Schlichenmaier, R., Bellot Rubio, L. R., et al. 2022, A&A, 666, A21
Reep, J. W., Bradshaw, S. J., & Alexander, D. 2015, ApJ, 808, 177
Rimmele, T. R., Warner, M., Keil, S. L., et al. 2020, Sol. Phys., 295, 172
Rubio da Costa, F., Kleint, L., Petrosian, V., Sainz Dalda, A., & Liu, W. 2015, ApJ, 804, 56
Rubio da Costa, F., Kleint, L., Petrosian, V., Liu, W., & Allred, J. C. 2016, ApJ, 827, 38
Ruiz Cobo, B., Quintero Noda, C., Gafeira, R., et al. 2022, A&A, 660, A37
Socas-Navarro, H., de la Cruz Rodríguez, J., Asensio Ramos, A., Trujillo Bueno, J., & Ruiz Cobo, B. 2015, A&A, 577, A7
Song, T.-F., Zhao, M.-Y., Zhang, X.-F., et al. 2024, SPIE, 13504, 1350409
Tei, A., Sakaue, T., Okamoto, T. J., et al. 2018, PASJ, 70, 100
Uitenbroek, H. 2001, ApJ, 557, 389
Vissers, G. J. M., Danilovic, S., de la Cruz Rodríguez, J., et al. 2021, A&A, 645, A1
von der Lühe, O. 1998, New Astron. Rev., 42, 493
Xu, Y., Cao, W., Ding, M., et al. 2016, ApJ, 819, 89
Yadav, R., Díaz Baso, C. J., de la Cruz Rodríguez, J., Calvo, F., & Morosin, R. 2021, A&A, 649, A106
Yadav, R., de la Cruz Rodríguez, J., Kerr, G. S., Díaz Baso, C. J., & Leenaarts, J. 2022, A&A, 665, A50
Zarro, D. M., Canfield, R. C., Strong, K. T., & Metcalf, T. R. 1988, ApJ, 324, 582